Synthesis, Crystal Structures, and Properties of Zeolite-Like $T_3(H_3O)_2[M(CN)_6]_2 \cdot u H_2O$ (T = Co, Zn; M = Ru, Os)

Leslie Reguera,*[a,b] Noeldris L. López,[b,c] Joelis Rodríguez-Hernández,[d] Marlene González,[e] Carlos E. Hernandez-Tamargo,[f,g] David Santos-Carballal,[f,h] Nora H. de Leeuw,[f,g,i] and Edilso Reguera*[a]

Abstract: We report the synthesis, crystal structures, and related properties of six new zeolite-like hexacyanometallates of formula unit $T_3(H_3O)_2[M(CN)_6]_2 \cdot u H_2O$ (T = Co^{2+}, Zn^{2+}; M = Ru^{II}, Os^{II}). Their crystal structures were solved and refined from their X-ray powder diffraction patterns in combination with the IR and UV/Vis/NIR spectroscopic data. The Co and Zn ions are coordinated tetrahedrally to the N atoms of four CN groups. The deconvolution of the overlapped UV/Vis/NIR spectral bands provided conclusive evidence of the tetrahedral coordination of the Co atoms. These materials have porous frameworks, which are characterized by a 3D array of TN_4 tetrahedral units linked to the MC_6 octahedral blocks in a 3:2 ratio. From the IR spectroscopy results, we found that all of the compounds reported here contain hydronium countercations. Two different structures in the same space group ($R\bar{3}c$) were identified for the Co-based materials. However, only a single phase was found for the Zn-containing compounds. Density functional theory (DFT) modeling predicts hydrogen bonds between the hydronium ions and the CN groups at the surfaces of the pores. These materials were prepared through the hydrothermal recrystallization of the solids obtained from mixing ethanol solutions of $H_4[M(CN)_6]$ with aqueous solutions of cobalt(II) nitrate and zinc nitrate. Our results illustrate the potential of the hydrothermal recrystallization technique for the preparation of metal hexacyanometallates with new structures and pore topologies that are not obtainable by the traditional precipitation method.

Introduction

During recent decades, transition-metal hexacyanometallates have received increasing attention because of their wide structural diversity and physical properties; for example, they have been used as prototypical nanoporous solids for hydrogen storage.[1] Their general formula unit is $(T^i)_x(A^j)_z[M^k(CN)_6]_y \cdot u H_2O$, in which T and M are transition metals; A is the countercation; the i, j, and k superscripts are the oxidation numbers; x, y, and z indicate the stoichiometry; and u is the hydration degree. In this family of solids, the M metal is always found in the low-spin state, and its oxidation state will be indicated with roman numerals (II). These solids form a 3D network of periodically repeated $\cdots N-T-N\equiv C-M-C\equiv N-T-N\cdots$ chains and are closely related to the Prussian blue (PB) analogues, in which all of the metal ions linked to the CN groups have octahedral geometries. The physical properties of these solids can be tuned through the variation of the transition metals or the application of an external stimulus such as light, pressure, temperature, or chemical potential. Thus, these materials find applications as molecular magnets;[2] sorbents[1,3] for gases such as H_2, CH_4, and CO_2; and ionic conductors.[4]

Their suitability for these applications has traditionally been rationalized in terms of the following: (1) The ability of the CN group to move electronic charge from the M to the T atoms. This involves π-back-donation from M to C and donation from the N atom to the T atom through a σ-bond; therefore, the electron clouds of all of these atoms overlap. (2) The topology of the material, which is dictated by the coordination number of the T metal and the presence of $[M(CN)_6]$ vacancies. The last two structural factors determine the formation of a porous framework with up to 50 % free volume,[5] which can accommodate guest molecules that modulate the material properties such as the magnetic behavior.[6] Hexacyanometallates usually crystallize in the cubic structure if the M and T metals have

[a] *Instituto Politécnico Nacional, Centro de Investigación en Ciencia Aplicada y Tecnología Avanzada, U. Legaria,*
Ciudad México, México
E-mail: edilso.reguera@gmail.com
[b] *Universidad de La Habana, Facultad de*
Química, La Habana, Cuba
E-mail: lesliereguera2005@gmail.com
[c] *Universidad de La Habana, Instituto de Ciencia y Tecnología de Materiales, La Habana, Cuba*
[d] *Centro de Investigación en Química*
Aplicada, Saltillo, Coahuila, México
[e] *CONACyT – Instituto Politécnico Nacional, Centro de Investigación en Ciencia Aplicada y Tecnología Avanzada, U. Legaria, Ciudad México, México*
[f] *School of Chemistry, Cardiff University, Main Building, Park Place, Cardiff CF10 3AT, United Kingdom*
[g] *Department of Chemistry, University College London, 20 Gordon Street, London, WC1H 0AJ, United Kingdom*
[h] *Materials Modelling Centre, School of Physical and Mineral Sciences, University of Limpopo, Private Bag x 1106, Sovenga 0727, South Africa*
[i] *Department of Earth Sciences, Utrecht University, Budapestlaan 4, 3584 CD Utrecht, The Netherlands*

octahedral coordination. However, tetrahedral coordination is also possible if one of the transition metals is Zn or Co that breaks the cubic symmetry of the crystal, which typically becomes rhombohedral.[7] For the low-symmetry structure, the electron-transfer mechanism from M–CN to the T metal through the 5σ orbital of the CN group is less favorable.[4b,8] This charge-transfer scheme determines the electronic properties of the cavity surface, the adsorption potential of the guest molecules,[1e] the mobility of the countercations,[4b] and the magnetic properties of these materials.[7d,9]

In this paper, we report the synthesis, crystal structures, and physical properties of the series $T_3(H_3O)_2[M(CN)_6]_2 \cdot uH_2O$ for T = Co^{2+}, Zn^{2+} and M = Ru^{II}, Os^{II}. To the best of our knowledge, this is the first report on the preparation and characterization of these compounds. These samples were prepared through the solvothermal recrystallization of low-crystallinity powders. These powders were precipitated by combining ethanol solutions of $H_4[M(CN)_6]$ synthesized in situ with aqueous solutions of Co^{2+} and Zn^{2+} salts. The geometry of the Co^{2+} ions was inferred from the UV/Vis/NIR spectra. The structures of the networks of water molecules within the framework cavities, including the role of the hydronium ions in the stabilization, were analyzed through IR spectroscopy and density functional theory (DFT) modeling. H_2 adsorption was used to probe the interactions between the hydronium ions and the cavity surfaces.

Results and Discussion

Crystal Structures

The experimental conditions used for the synthesis of the materials studied here are summarized in Table 1. The S and L labels for the Co-based cyanometallates correspond to the structures with the smaller and larger cell volume, respectively. From the XRD patterns, we found that two Co-based phases were formed for each inner metal (Ru, Os). However, for Zn, only a single phase was identified for each inner metal. Regardless of the composition, all phases crystallized in a rhombohedral unit cell with the space group $R\bar{3}c$. From the cell parameters and the cell volume per formula unit (see Table 2), we concluded that the Zn-based hexacyanometallates only crystallize in the S phase. This finding is further supported by the structural similarities between the Co- and Zn-based S phases and the previously reported $Zn_3A_2[M(CN)_6]_2 \cdot uH_2O$ counterpart with A = Na,

Table 1. Hydrothermal recrystallization conditions.

Sample composition[a]	$Co_3(H_3O)_2[M(CN)_6]_2 \cdot yH_2O$ (M = Ru^{II}, Os^{II})	$T_3(H_3O)_2[Ru(CN)_6]_2 \cdot xH_2O$ (T = Co^{2+}, Zn^{2+})	$T_3(H_3O)_2[Os(CN)_6]_2 \cdot xH_2O$ (T = Co^{2+}, Zn^{2+})
Label	Co_3M_2 L phase	T_3Ru_2 S phase	T_3Os_2 S phase
Experimental conditions	Co(NO₃)₂ aq. solution (0.03 M), 130 °C, 7 d	HCl aq. solution (1.25 M), 130 °C, 48 h	HCl aq. solution (1 M), 105 °C, 48 h

[a] Hydration degree: $y > x$ for all the samples. Note that we have labeled the hydration degree as y for the L phases and x for the S phases.

Table 2. Experimental (exp.) and calculated (calcd.) values for the lattice parameters (in the hexagonal representation), cell volume per formula unit, and bond lengths and angles for the hexacyanometallates under study.[a]

Compound	Lattice parameters [Å]		Cell volume per formula unit [Å³]		Bond lengths [Å] T–N		Bond angles [°] T–N–C		M–C–N		N–T–N	
	exp.	calcd.	exp.	calcd.	exp.	calcd.	exp.	calcd.	exp.	calcd.	exp.	calcd.
$Co_3(H_3O)_2[Ru(CN)_6]_2 \cdot 7.9H_2O$ L phase	a = b = 12.567(4) c = 35.704(5)	a = 12.720 b = 12.168 c = 32.936	4883.5(2)	4447.3	2.131(3) 2.066(7)	2.022 1.931	164.2(3) 164.2(2)	136.7 160.4	173.6(1) 172.5(2)	172.4 174.9	110.9(3) 116.6(5) 107.6(2) 102.8(3)	109.3 ± 6.9 109.4 ± 3.8
$Co_3(H_3O)_2[Os(CN)_6]_2 \cdot 8.4H_2O$ L phase	a = b = 12.579(3) c = 35.647(5)	a = 12.710 b = 12.639 c = 33.513	4885.0(3)	4530.9	2.117(3) 2.100(7)	2.004 1.925	161.8(1) 164.1(2)	139.4 162.4	172.5(1) 170.1(2)	173.2 176.0	112.0(10) 115.0(5) 106.6(2) 104.2(7)	109.3 ± 6.5 –
$Co_3(H_3O)_2[Ru(CN)_6]_2 \cdot 5.8H_2O$ S phase	a = b = 12.829(3) c = 33.505(3)	a = 12.746 b = 12.143 c = 32.477	4781.6(2)	4393.8	2.013(3) 2.024(7)	2.012 1.926	160.1(1) 159.4(2)	139.1 160.4	178.4(1) 179.5(2)	173.1 174.3	105.7(10) 113.9(5) 110.2(2) 106.5(7)	109.4 ± 7.0 109.4 ± 3.3
$Co_3(H_3O)_2[Os(CN)_6]_2 \cdot 6.8H_2O$ S phase	a = b = 12.810(3) c = 33.451(5)	a = 12.685 b = 12.531 c = 33.857	4753.7(2)	4511.8	2.015(3) 2.017(7)	1.997 1.924	160.1(1) 159.4(2)	139.6 161.1	178.5(1) 179.6(2)	172.6 175.5	105.4(10) 113.9(5) 110.5(2) 106.5(7)	109.4 ± 6.9 –
$Zn_3(H_3O)_2[Ru(CN)_6]_2 \cdot 5.2H_2O$ S phase	a = b = 12.818(2) c = 33.483(3)	a = 12.744 b = 12.186 c = 32.341	4764.3(3)	4367.0	2.012(3) 2.023(7)	2.025 1.917	160.1(1) 159.4(2)	138.0 158.5	178.4(1) 179.5(2)	172.7 174.9	105.7(10) 113.9(5) 110.2(2) 106.5(7)	109.2 ± 7.4 109.4 ± 2.4
$Zn_3(H_3O)_2[Os(CN)_6]_2 \cdot 6.9H_2O$ S phase	a = b = 12.827(2) c = 33.327(3)	a = 12.698 b = 12.637 c = 34.550	4749.1(3)	4748.7	2.007(3) 2.023(7)	2.230 1.927	159.9(1) 159.5(2)	140.0 160.3	178.4(1) 179.5(2)	172.8 175.7	105.5(6) 106.7(5) 110.2(2) 113.9(7)	109.3 ± 6.7 109.4 ± 4.1

[a] Two average values are listed for each calculated bond length and angle: the upper value corresponds to N atoms forming hydrogen bonds with hydronium ions, while the lower value corresponds to N atoms with no hydrogen bonds. If at least one N atom of each tetrahedron is forming one hydrogen bond with a hydronium ion, only one value is listed for the N–T–N angle. The standard deviation of the N–T–N angle is listed as a measure of the tetrahedron distortion.

K, Rb, and Cs.[7d,7e] The alkali-metal-based series has an open-framework structure of six ellipsoidal cavities per hexagonal unit cell, connected through an elliptical windows of ca. 6.8 × 8 Å. The position of the countercation (A^+) in the alkali-metal-based systems, lying close to the corners of the ZnN_4 unit,[1d,1e,7d,7e] suggests that the hydronium ions interact with the N atoms owing to the accumulation of negative charge on these atoms. The presence of hydronium countercations for all of the materials studied here is clearly expected, as the source of the hexacyanometallate units was the $H_4[M(CN)_6]$ acid com-plex.

High-quality XRD powder patterns were used for the crystal-structure refinement by the Rietveld method,[10] and the struc-ture of $Zn_3A_2[M(CN)_6]_2 \cdot xH_2O$[7a] was used as the starting point. The calculated XRD patterns for the refined structures compare well with the experimental ones (Figure 1 and Supporting Infor-mation). Moreover, the UV/Vis/NIR and IR spectra along with the thermogravimetric (TG) and H_2 adsorption data also lend support to the refined crystal structures (discussed in the Hydrogen Adsorption section). For the refined crystal structures, we found that the T atom has a tetrahedral coordination to the cyanide N atoms, whereas the M inner metal atom preserves the octahedral coordination. Two types of water molecules were identified within the cavities, those presumably proto-nated and close to the tetrahedral TN_4 corners and others that form clusters stabilized through hydrogen bonds. The deconvo-lution of the ν(O–H) vibrational bands in the IR spectra also supports the existence of such a network of hydrogen-bonded water molecules (discussed below). The packing of the water molecules within the porous frameworks for both the S and L phases is shown in Figure 2. The refined occupation factors of
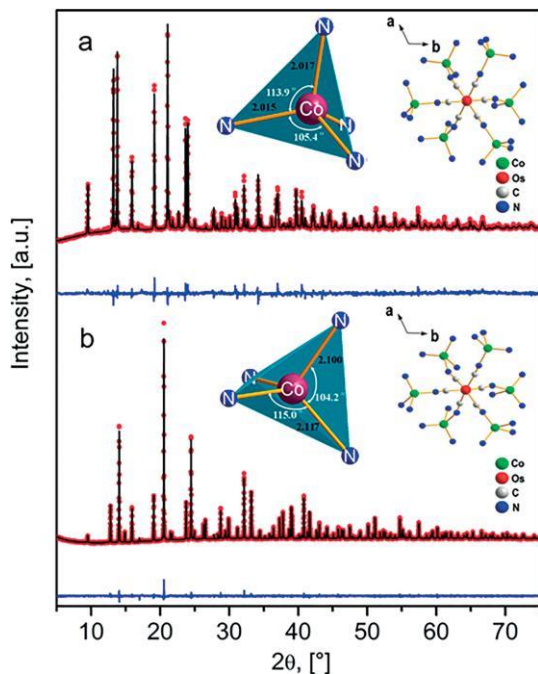

Figure 1. Observed (red) and calculated (black) XRD powder patterns and difference profiles (blue) for the Rietveld refinements of (a) $Co_3(H_3O)_2$-$[Os(CN)_6]_2 \cdot 6.8H_2O$ (S phase) and (b) $Co_3(H_3O)_2[Os(CN)_6]_2 \cdot 8.4H_2O$ (L phase). The insets show the coordination environments for the T metals.

the cavity sites, available for water molecules, are also in excel-lent agreement with the hydration degrees obtained through the TG analysis. To confirm the tetrahedral coordination for the Co atoms, we deconvoluted the UV/Vis bands according to the ligand-field theory (discussed below).
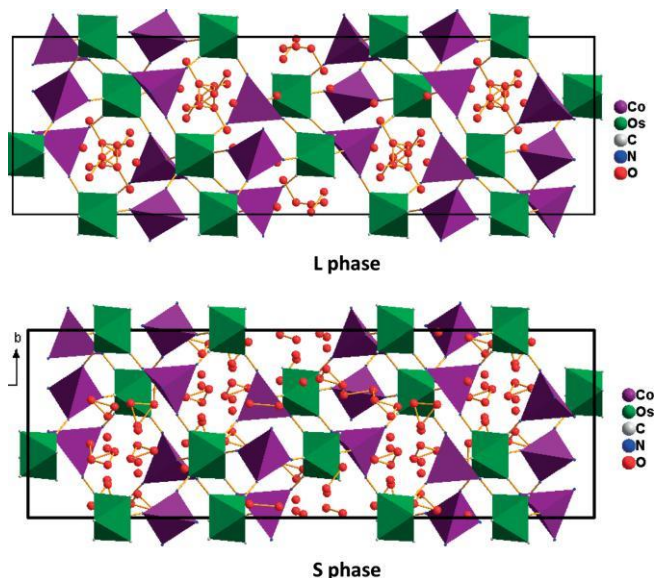

Figure 2. Packing of oxygen atoms within the framework for the S and L phases of $Co_3(H_3O)_2[M(CN)_6]_2 \cdot uH_2O$ for M = Ru and Os.

For all cases, our results indicate that the geometry of the TN_4 tetrahedron deviates from the ideal one, for which the bond angle is 109.5°(see Figure 1, Table 2, and Supporting Infor-mation). Such deviations are more pronounced for the L phase where the bond angles estimated for Ru are in the 102.8–116.6° range, and those for Os range from 104.2 to 115.0° (see Figure 1 and Supporting Information). The L phase also has a larger cell volume per formula unit (2.13 % for Ru and 2.76 % for Os) than the S phase.

As shown clearly in Table 2, the main structural differences between the S and L phases lies in the M–C–N and C–N–T an-gles. Thus, the highest occupied molecular orbital (HOMO) from the CN group is not oriented towards the T metal, as the C–N– T angle is not linear. This leads to the localization of negative charge on the N atom, in agreement with previous reports.[4b,8] This accumulation of negative charge at the cavity surface de-termines the strength of the framework–water interactions and the water–water interactions through hydrogen bonds, which is known for zeolites.[11]

The refinement of our crystal structures and the TG experi-ments (discussed in the Thermal Behavior section) show that the L phases have the largest hydration degree. We found clus-ters of water molecules at the centers of the cavities of the L phases and chains of water molecules within the cavities of the S phases (see Figure 2). Note that Figure 2 was constructed from XRD experiments, a technique that cannot detect hydrogen atoms. Thus, we have assumed that the proton from the hydronium cation is randomly attached to the water mol-ecules. As also shown in Table 2, the T–N bonds are longer for

the L phase than for the S phase, reducing further the electronic donation from the CN group to the T metal center for the L-phase compounds. For further information, the refined atomic positions, occupation and thermal factors, along with the experimental and calculated bond lengths and angles are reported in the Supporting Information, and the CIF files are available from the Inorganic Crystal Structure Database (ICSD).

DFT Simulations

The structural parameters for the ab-initio-optimized geome-tries of the $T_3(H_3O)_2[M(CN)_6]_2 \cdot H_2O$ materials are listed in Table 2. As expected from the experimental results, the S phases have a smaller cell volume per formula unit than the L phases. All of the cell volumes per formula unit were moderately underesti-mated by our calculations, because we considered a single wa-ter molecule in them. However, the simulations were still able to predict larger cell volumes per formula unit for the Os-based compounds than for their Ru-containing counterparts. We found that all of the conventional unit cells broke the hexago-nal symmetry and became slightly trigonal. The relaxed lattice parameters were more deviated for the Os systems than for the Ru-based systems, whereas it was the other way around for the cell angles. As our computational model captures the main differences observed experimentally for the unit cells of these cyanometallates, we are confident of our DFT-predicted struc-tural, electronic, and magnetic properties.

From our simulations, we inferred that the bond angle for the tetrahedral atom (N–T–N) is more affected than that for the octahedral one (C–M–C), in agreement with the experimental results. We found that the M–C–N angle is essentially linear, whereas the T–N–C angle loses linearity if the N atom forms a hydrogen bond. Although the water and hydronium H atoms are oriented towards the cyanide N atoms, only the charged species are able to form hydrogen bonds. Interestingly, this sup-ports the idea that hydronium cations will bind to the surfaces of the pores and suggests that water molecules may form agglomerates through hydrogen bonds. We observed that hydrogen bonding was an important source of distortion for the T-centered tetrahedra. The standard deviation of the N–T– N angle was taken as a measure of the deformation[12] and reached values between 6.5 and 7.4° if strong CN–H interactions were established and decreased to 2.4– 4.1° for tetrahedra with no hydrogen bonds. In general, each hydronium ion was in-volved in at least two hydrogen bonds; therefore, most of the

tetrahedra were affected by the presence of the counterions. Although we only considered one water molecule per formula unit in our calculations; in the experiments, the effi-ciency of the framework distortion caused by a larger number of hydrogen bonding is expected to be smaller.

Thermal Behavior

For all of the L-phase materials, the weakly bonded clusters of water molecules evolve on heating before 120 °C. Then, the samples do not experience any significant mass losses until 420 °C, which is the decomposition temperature (see Support-ing Information). This suggests that the water molecules form-ing the hydronium ions remain strongly bonded to the surface of the cavities until the thermal decomposition of the materials occurs.[13] On the other hand, all of the S-phase cyanometal-lates show quite different thermal behavior. Unlike those of the L phase, the hydrogen-bonded water molecules evolve progres-sively at higher temperatures. This suggests a broader distribu-tion of the strength of the hydrogen-bond interactions for the S-phase materials and substantiates the formation of chains of water molecules within the cavities.

The highest thermal stabilities were observed for the Os-based cyanometallates. Osmium has a larger atomic radius with more extended t$_{2g}$ orbitals and less electronegativity than Ru allowing a better π-back-donation. Therefore, a larger negative charge density accumulates at the surfaces of the cavities en-hancing the interactions of the framework with the water mol-ecules and the thermal stability of the materials. The TG curves for all of the materials under study are shown in the Supporting Information.

IR Spectra

The IR spectra of the hexacyanometallates are dominated by the stretching mode (ν) of the C–N, C–M, and O–H bonds and the bending mode (δ) of the MCN and HOH groups (see Table 3). Note that the ν(OH) and δ(HOH) vibrational modes reveal the presence of water molecules and hydronium ions in the porous frameworks of these materials. The two partially resolved δ(HOH) bending modes suggest that the water mol-ecules are in slightly different environments within the frame-work cavities. The broadening of the ν(OH) band indicates the formation of hydrogen bonds within either the water clusters or chains. The O–H stretching spectral region was deconvoluted

Table 3. IR absorption bands [cm^{-1}] and dehydration temperature T_D [°C] for the studied compounds. The presented vibrational modes are the stretching (ν) and bending (δ) modes. The frequencies for the ν(OH) individual bands were estimated from the deconvolution of the bands in the range $\tilde{\nu}$ = 3800–2775 cm^{-1}. See Supporting Information.

Compound	ν(CN)	δ(MCN)	ν(MC)	ν(OH)	δ(H₂O)[a]	T_D
Co₃Ru₂ L phase	2088	556	467	3649, 3621, 3555,3455, 3334, 3205, 3096	1636, 1603	113
Co₃Os₂ L phase	2075	552	481	3659, 3632, 3621, 3504, 3375, 3202, 3178	1639, 1603	110
Co₃Ru₂ S phase	2092	557	463	3631, 3574, 3480, 3425, 3204, 3114, 3002	1625, 1611(sh)	124
Co₃Os₂ S phase	2088	552	477	3358, 3212, 3116, 3003	1627, 1611 (sh)	134
Zn₃Ru₂ S phase	2105	557	461	3273, 3200, 3110, 2926	1613	102
Zn₃Os₂ S phase	2092	552	477	3633, 3575, 3475, 3424, 3209, 3115, 3006	1624 (sh),1612	116

[a] sh: shoulder.

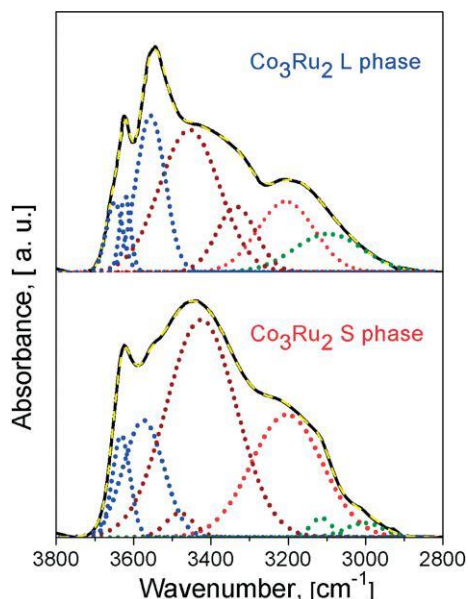to provide further information on the water molecules (Figure 3).

Figure 3. Deconvolution of the O–H stretching (ν) spectral region for the L and S phases of Co3Ru2. Similar deconvolution patterns were obtained for the remaining compositions (see Supporting Information). Such a deconvolution model is in accordance with the accepted model for hydrogen-bonded water clusters.[14]

The frequency for the ν(CN) vibrational mode provides an indication of the valence and coordination geometry of both the M and T metals in hexacyanometallates.[7d,15] As shown in Table 3, the lowest-wavenumber ν(CN) bands correspond to the Os-based materials implying weaker CN bonds. The weakening of the CN bonds can be rationalized in terms of the population of the lowest unoccupied molecular orbital (LUMO) owing to strong π-backbonding from the Os atom (see Table 3). Our IR experiments also show that the ν(CN) band for the Zn-based compounds is blueshifted with respect to those of the other cyanometallates. This implies a strengthening of the CN bond, in agreement with the higher Lewis acidity of Zn^{2+} ions com-pared with Co^{2+} ions. We were unable to detect the ν(NT) bands as they typically appear below the lowest recording limit of the instrument used.

UV/Vis/NIR Spectra – Ligand-Field Analysis

The UV/Vis/NIR diffuse reflectance spectra were recorded in the energy range between 8000 and 50000 cm^{-1}. In Table 4, the absorption bands are listed in three groups: (1) the charge transfer from the M metal to the CN ligand, (2) the d–d transitions for the M metal with low-spin d^6 electronic configuration, and (3) the d–d transitions of Co^{2+} ions with a high-spin[7] electronic configuration. For the Zn^{2+} ions with a d^{10} closed-shell configuration, only the first two groups of transitions are al-lowed and are strongly overlapped. We found that the energy of the d–d transitions of the inner metal atom decreased for both phases from Ru to Os, and this suggests that the NC–Os bond has a weaker ligand-field interaction. As discussed previ-ously for the thermal stability of these materials, this behavior is expected because of the different size and electronegativity of the Ru and Os atoms. The d–d transitions for the Co^{2+} ion are highly sensitive to the geometry of the coordination envi-ronment and depend on the S or L phase and the Co–N–C bond angle of the formed structure (see Figure 4 and Table 4).

The ligand-field analysis (LFA) of the UV/Vis/NIR absorption spectra provides information on: (1) the coordination number and symmetry of the metal centers through the number of

Table 4. UV/Vis/NIR absorption bands [cm^{-1}], Racah parameters [cm^{-1}], 10 Dq parameters [cm^{-1}], and band gaps E_g [eV] estimated from the Tauc plots. The ab initio band-gap values are provided in parentheses.

Assignments	Co3Ru2 L phase	Co3Os2 L phase	Co3Ru2 S phase	Co3Os2 S phase	Zn3Ru2 S phase	Zn3Os2 S phase
d-d T^{2+}						
$^4A_2 \rightarrow {}^4T_1(F)$	7629, 8599	7174, 9013	7819, 9247	7755, 9910		
$^4A_2 \rightarrow {}^2E(G)$	15766	13604	15602	15297		
$^4A_2 \rightarrow {}^2T_1(G)$		15595		15755		
$^4A_2 \rightarrow {}^4T_1(P)$	16552, 17953	16530, 18006	16244, 17914	16822, 18460		
$^4A_2 \rightarrow {}^2A_1(G)$	19458	18025	16994	20218		
$^4A_2 \rightarrow {}^2T_2(G)$			20083			
$^4A_2 \rightarrow {}^2A_2(F)$	–	–	21539	–		
Racah parameter						
$\bar{B}$	742	744	702	722		
$10\,\bar{D}_q$	4728	4723	5016	5203		
d-d M^{II}						
$^1A_{1g} \rightarrow {}^3T_{1g}$	26921	24475	26501	23810	–	28264
$^1A_{1g} \rightarrow {}^3T_{2g}$	28741	26014	28307	24533	30328	28967
$^1A_{1g} \rightarrow {}^1T_{1g}$	32470	29318	31542	27231	35112	34821
$^1A_{1g} \rightarrow {}^1T_{2g}$	40479	–	38681	34512	–	39317
Racah parameters						
B	501	nd	446	455	nd	281
C	2775	2422	2521	1711	nd	3278
$10\,D_q$	35245	31740	34063	28942	nd	38009
Ch. T. M $\rightarrow$CN						
$A_{1g} \rightarrow T_{1u}^{(1)}$	46158	42679	50063	45557	42522	42112
$A_{1g} \rightarrow T_{1u}^{(2)}$	–	–	–	–	48636	48431
E_g	3.21 (2.71)	2.86 (2.61)	3.14 (2.70)	2.73 (2.75)	3.74 (3.28)	3.49 (3.34)

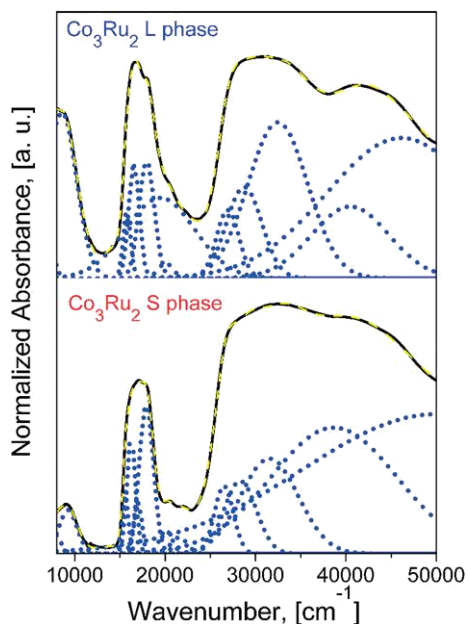nd: insufficient data to determine the value

Figure 4. Deconvolution of UV/Vis/NIR spectra for the L and S phases of Co$_3$Ru$_2$ according to the ligand-field theory.[16]

d–d transitions and their energies, (2) the ligand-field strength at the internal and external metal atoms from the value of the ligand-field splitting energy (10 Dq); and (3) the covalent char-acter of the coordination bonds from the value for the Racah parameter B.

The effect of the symmetry distortion is more notable for the Co^{2+} center (d^7), because it splits the T_d tetrahedral d–d excitations into multiple transitions (see Table 4). Note that for the analysis of the electronic transitions of all metal atoms, we ignored the small distortion from the ideal O_h or T_d symmetry for the internal and external metal atoms, respectively, in line with previous work.[14] For the tetrahedral Co^{2+} ions, the ground state is the ^{4}A term, which is followed by three accessible excited states of the same multiplicity: ^{4}T$_2$, ^{4}T$_1$(^{4}F), and ^{4}T$_1$(^{4}P) in order of increasing energy. The low-energy ^{4}A–^{4}T$_2$ transition is not reported in this work, because it appears below the lowest limit of detection of the instrument used. The ^{4}A–^{4}T$_1$(^{4}F) transition has a low energy, and its appearance together with multi-ple ^{4}A–^{4}T$_1$(^{4}P) absorption bands in the near-infrared and visible regions, respectively,[16] provides conclusive proof of the tetrahedral coordination of the Co^{2+}ion. The transitions with the highest energies, namely ^{4}A–^{4}T$_1$(^{4}F) and ^{4}A–^{4}T$_1$(^{4}P), are split into two bands centered in the energy ranges $\tilde{v}$ = 7000 to 10000 (NIR region) and 16500 to 18500 cm^{-1} (visible region), respectively (see Table 4). The Co transitions in the visible region are spin-forbidden quartet–doublet bands, which widen and gain intensity through interactions with the spin-allowed band in the visible region.

For the octahedral Ru^{II} and Os^{II} ions in a strong ligand field, the ground state is the ^{1}A$_{1g}$ term, which is followed by five accessible excited states of the same multiplicity. However, of the five possible transitions, we were only able to observe two spin-allowed transitions below $\tilde{v}$ = 50000 cm^{-1}, ^{1}A$_{1g}$→^{1}T$_{1g}$(^{1}I) and ^{1}A$_{1g}$→^{1}T$_{2g}$(^{1}I), in addition to two spin-forbidden transitions,

that is, ^{1}A$_{1g}$→^{3}T$_{1g}$(^{3}H) and ^{1}A$_{1g}$→^{3}T$_{2g}$(^{3}H) (see Table 4). We found that all M metal d–d transition bands overlapped strongly with the metal-to-ligand charge-transfer bands.

The smallest Racah B parameters (relative to the Co–N bond), calculated from the UV/Vis/NIR spectra, were found for the com-pounds with the S phase indicating a higher covalent degree for the Co–N bond (see Table 4). From a molecular-orbital point of view, this suggests that the ligand-to-metal σ-donation from the N to the T atom is favored in the S-phase compounds. Such a prediction from the electronic spectra is supported by the previously discussed data from IR spectroscopy, TG analysis, and the structural study. The smaller values found for the B parame-ter for the four Co-containing compositions (see Table 4) than that for the free Co^{2+} ion (B = 956 cm^{-1})[17] imply a higher covalent character for the T–N bonds of the Co-based com-pounds. Moreover, the largest ligand-field-splitting energies (10 Dq) of the Co–N bond were measured for the materials with the S phase, in agreement with their larger N-to-Co charge transfer.

The largest 10 Dq values for the M–C bonds of both phases of the Ru-based compounds (see Table 4) indicates better li-gand-to-metal σ-donation, whereas the lower electronegativity of Os favors the M metal-to-ligand π-donation (with respect to the M–C bond).

Band-Gap Energies

Metal hexacyanometallates behave as wide-band-gap (E_g) semi-conductor materials, and the value of E_g depends on the M and T metals and on the crystal structure of the material.[18] In this work, we estimated the E_g values by applying the standard pro-cedure[19] of extrapolating to zero the following linear function obtained from the UV/Vis/NIR absorption [Equation (1)]:

$$[F(R)h\nu]^2 = C(h\nu - E_g) \qquad (1)$$

$F(R)$ is the so-called remission or Kubelka–Munk function, $R = R_{sample}/R_{standard}$, C is a proportionality constant, and $h\nu$ is the photon energy.[20] The calculated E_g values are also included in Table 4. For all compositions and phases, the smallest E_g values correspond to the Os-containing solids. As discussed previously, Os is a bulky metal with diffuse t$_{2g}$ orbitals, which favor the π-back-donation to the CN ligands, which reduces the band-gap energy.

Magnetic Properties

Ru^{II} and Os^{II} ions have a t$_{2g\uparrow}$^{3}t$_{2g\downarrow}$^{3} low-spin electronic configura-tion preventing contributions to the magnetic properties of the materials. The Zn^{2+} ion is a closed-shell ion with a 3d^{10} elec-tronic configuration and cannot contribute to the overall mag-netic properties of these materials. However, Co^{2+} ions are para-magnetic with an e$_\uparrow$^{2}e$_\downarrow$^{2}t$_{2\uparrow}$^{3} electronic distribution. The tem-perature dependence of the effective magnetic moment (μ_{eff}) for the Co-based compounds calculated according to μ_{eff} = 2.828($_M T$)$^{1/2}$ is shown in Figure 5. The four materials show par-amagnetic character for the whole temperature range between 2 and 350 K. The sharp reduction for the μ_{eff} value at low tem-

perature suggests the presence of a weak antiferromagnetic coupling between the Co^{2+} spin carriers. This coupling occurs through the $\cdots Co–N\equiv C–M–C\equiv N–Co\cdots$ chain, in agreement with the negative values calculated for the J superexchange integral and the Curie–Weiss (θ_{CW}) constant (see Table 5).
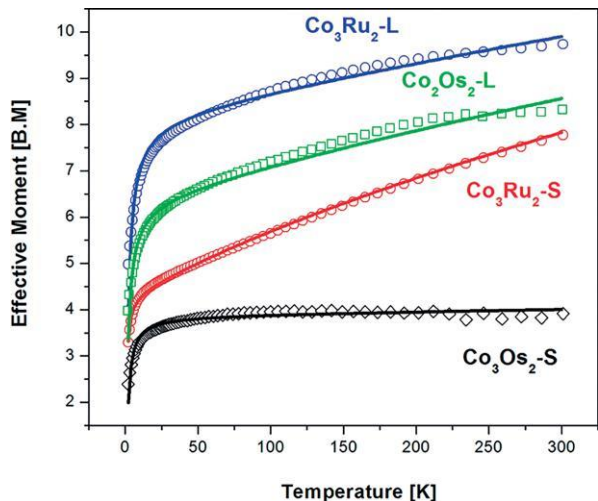

Figure 5. Temperature dependence of μ_{eff} for the $Co_3(H_3O)_2[M(CN)_6]_2 \cdot xH_2O$ compounds (M = Ru, Os).

Table 5. Parameters fitted with the MagSaki[22] software for an isotropic tetra-hedral environment and TIP contributions to the magnetic moment.

Sample	J [cm^{-1}]	g	θ [K]	TIP	Residual R (μ)
Co$_3$Ru$_2$-L	−0.6	4.2	−2.3	0.01358	0.000494
Co$_3$Os$_2$-L	−0.49	3.27	−2.2	0.014	0.000379
Co$_3$Ru$_2$-S	−0.4	2.2	−0.2	0.018	0.000063
Co$_3$Os$_2$-S	−0.756	2.001	−1.2	0.000484	0.000553

With the exception of that of the Co$_3$Os$_2$-S compound, the magnetic moments exceed the expected value of 6.63 µB above 200 K (see Figure 5). This paramagnetic character is temperature-dependent regardless of the spin–orbit coupling. The temperature dependence for μ_{eff} close to room temperature shows a certain tendency to the saturation value for all compositions. This suggests that temperature-independent paramagnetism (TIP) takes place for the orbital contribution and indicates the existence of low-lying electronic excited states. This is an expected behavior, because the contribution from the orbital momentum to the high-spin Co^{2+} state is not completely quenched for a perfect tetrahedral symmetry.[21]

To verify the contribution of the spin–orbit coupling and TIP to the magnetic moment, we fitted the magnetic data for two Co^{2+} ions in tetrahedral coordination environments with a weak magnetic interaction between them. The μ_{eff} versus temperature fitting was performed with the MagSaki software.[22] The system can be approximated as two paramagnetic Co centers with a weak antiferromagnetic interaction through the $\cdots Co–N\equiv C–M–C\equiv N–Co\cdots$ chains. The fitted and experimental μ_{eff} versus temperature curves are shown in Figure 5, and the fitted parameters are reported in Table 5. The model reproduces the experimental data at low temperature for the four compositions but deviates at high temperatures for the L phases. The reason

for the deviation is that a perfect tetrahedron was considered for the Co^{2+} ions in the model instead of a distorted tetrahedral coordination. The tetrahedral distortion is more pronounced for the Co-based L phases, in agreement with a larger deviation between the experimental and fitted curves. Therefore, the population of the excited states at high temperature increases the magnetic anisotropy as a result of the distortion of the Co coordination. For this analysis, we assumed that the energy separation of the excited states is in the kT order. From Figure 5, we see that the μ_{eff} value decreases on cooling as the kT value is smaller and the excited states become less accessible. Furthermore, the calculated TIP contribution is negligible, in correspondence with the experimental evidence, whereas the variation for the g value is congruent with an increasing spin–orbit contribution to the magnetic moment (see Table 5 and Figure 5).

In the UV/Vis/NIR spectra, the last Co electronic transition [$^4T_1(P)\leftarrow {}^4A_2(\nu3)$] is observed in the visible region. This is the reason for the crystal-field contribution to the magnetic anisot-ropy around the Co^{2+} ion. The experimental magnetic data are in agreement with the refined crystal structures and the struc-tural information derived from the UV/Vis spectra.

Electronic and Magnetic Properties

The Bader analysis indicates that the charge transfer is negligible between the water molecules and the inner surfaces of the materials. However, the hydronium ions gain electronic charge from the nearby N atoms and become nearly neutral. The total magnetization of saturation (M_S) was calculated at 9.00 µB per formula unit (f.u.) from the atomic spin moments (m_S) of the Co-based cyanometallates. Our simulations also confirmed that the Zn-containing materials are nonmagnetic. For all of these compounds, m_S(Co) = 3.00 µB, which is in good agreement with the electronic distribution of the Co^{2+} ions, that is, $e_\uparrow^2 e_\downarrow^2 t_{2\uparrow}^3$. On the other hand, Zn has a closed-shell electronic distribution, and M has a $t_{2g\uparrow}^3 t_{2g\downarrow}^3$ low-spin configuration; therefore, these atoms are nonmagnetic. In all cases, the total magnetization of saturation has an integer value, which indicates that the materials have a band gap in at least one of the spin channels.[23] It should be noted that the experimental M_S(Co$_3$Os$_2$-S) is approximately 4 µB/f.u. We speculate that certain domains within the crystal of this compound have a different magnetic structure, which corresponds to an antiparallel (antiferromagnetic) alignment of the magnetic moments of the Co atoms. Although this may be driven by the weak negative superexchange interaction measured experimentally between the Co atoms through the $\cdots Co–N\equiv C–M–C\equiv N–Co\cdots$ chain, this situation is outside the scope of this paper. However, for comparison, we treated all of the systems computationally as ferromagnets with the atomic spin moments aligned in the same direction and did not con-sider competing magnetic domains.

Hydrogen Adsorption

The hydrogen molecule has a relatively small kinetic diameter (2.86 Å), which facilitates its diffusion through small windows

and narrow channels. In the absence of partially naked metal centers, the hydrogen adsorption process is dominated by elec-trostatic interactions.[24] These interactions result from the elec-tric field gradient with the H_2 quadrupole moment and the po-larization of this molecule by a charge center and have r^{-3} and r^{-4} dependences, respectively (r is the distance between the involved electron clouds).[25] Such interactions make it possible to use the H_2 adsorption isotherm to probe the local electric field gradient inside the cavities of the material. The local field gradient is determined by the negative-charge concentration at the surfaces of the cavities and the effective polarizing power of the countercation.[1d,1e]

The low-pressure region of the H_2 adsorption isotherms recorded at 75 K is shown in Figure 6. The slope of the adsorption isotherm at low pressure (low surface coverage of the adsor-bate molecules) provides a measure of the strength of the host–guest interactions (adsorption forces). On the basis of the slopes of these isotherms, the strength for the host–guest inter-action follows the order Co_3Os_2-S > Co_3Ru_2-S > Co_3Os_2-L > Co_3Ru_2-L, which is in agreement with the TG and IR spectro-scopy results. The strong electrostatic interactions between the negative charge density at the surface of the cavity and the hydronium ion reduces the effective polarizing power of the cation and weakens the adsorption potential for the H_2 mol-ecule. For the S phase, in which the hydronium ion preserves its high polarizing power, the stabilization of the H_2 molecule within the cavity is favored. For the Zn-based compounds, the order for the host–guest interactions is Zn_3Os_2 > Zn_3Ru_2, owing to the higher charge-density concentration at the cavity surface of the Os-containing compound. For more information, the H_2 adsorption isotherms recorded at 75 K and up to 5 bar as well as the curve fits for a combination of low- and high-pressure models are available in the Supporting Information.
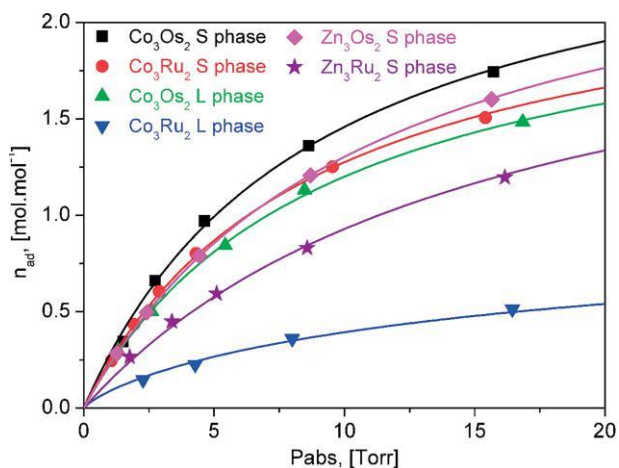

Figure 6. Low-pressure region (< 20 Torr) for the H_2 adsorption isotherms of the $T_3(H_3O)_2[M(CN)_6]$·uH_2O series at 75 K.

Conclusions

The series $T_3(H_3O)_2[M(CN)_6]_2$·xH_2O (T = Co^{2+}, Zn^{2+}; M = Ru^{II}, Os^{II}) crystallizes in a rhombohedral unit cell with the $R\bar{3}c$ space group. The porous framework of these materials is formed by a

3D array of MC_6 octahedra and slightly distorted TN_4 tetra-hedra. For T = Co, two structural modifications were identified with different cell volumes per formula unit. In these com-pounds, the hydronium ions are the countercations and are lo-cated close to the corners of the tetrahedra. The free volume in the structure is partially occupied by weakly bonded water molecules stabilized within the cavity through hydrogen-bond interactions with the hydronium ions. Two structures of weakly bonded water molecules were identified, that is, clusters and chains. The clusters are formed when the polarizing power of the hydronium ion is reduced by the negative charge of the cavity. In this case, the stabilization of the water molecules within the cavity is dominated by the formation of hydrogen bonds between them. If the hydronium ion is able to preserve a high polarizing ability, the water molecules form chains. Con-clusive information in this regard was obtained from the decon-volution of the ν(OH) region of the IR spectra and from theoreti-cal calculations. The TG curves confirmed the presence of these two types of structures of water molecules. The H_2 isotherms, recorded after the removal of the weakly bonded water mol-ecules, provide an indication for the effective polarizing power of the hydronium ion. The crystal-field analysis of the recorded UV/Vis/NIR spectra, the $_MT$ versus T graphs, and the DFT simu-lations provided conclusive proof of the distortion of the Co coordination environment. This study revealed that the hydro-thermal recrystallization method is a convenient route to im-prove the crystallinity of metal hexacyanometallates, which are usually obtained as fine powders.

Experimental Section

Six materials with the general composition $T_3(H_3O)_2[M(CN)_6]_2$·xH_2O (T = Zn^{2+}, Co^{2+} and M = Ru^{II}, Os^{II}) were prepared by the hydrother-mal recrystallization of four crude solids obtained by adding an ethanol solution (0.03 M, 25 mL) of $H_4M(CN)_6$ dropwise to an aque-ous solution (0.01 M, 250 mL) of $T(NO_3)_2$. The precipitate formed was aged in the mother liquor for 24 h, then separated by centrifu-gation, and washed several times with distilled water to remove all of the accompanying ions. Finally, each solid was divided into two equal parts and transferred to Teflon-sealed autoclave flasks for the hydrothermal recrystallization (see Table 1). The resulting solids were washed again several times with distilled water and then sepa-rated and air-dried to a constant weight. Six polycrystalline materi-als appropriate for the structural study were obtained. The fine powders obtained from the primary precipitation process were ma-terials of poor crystallinity. The $H_4M(CN)_6$ solutions used during the synthesis were prepared in situ[26] from potassium hexacyano-ruthenate(II) and hexacyanoosmate(II). The hexacyano complexes were synthesized from $RuCl_2$·H_2O or OsO_4 and KCN according to previously reported procedures.[1e]

The nature of the obtained solids was established through energy-dispersive spectroscopy (EDS), powder XRD, IR spectroscopy, UV/ Vis/NIR spectroscopy, and magnetic data. The hydration degree and thermal stability were evaluated by thermogravimetric analysis. From the EDS spectra, the ratios of the metal atoms (T/M) for these materials were close to 3:2, without the presence of any other metal. The deconvolution of the IR bands for the ν(OH) vibrations provided conclusive evidence of the presence of hydronium coun-tercations and their interactions with the cavity surface and water molecules within the cavity.

TG curves were recorded in the 30–300 °C interval under N_2 (100 mL/min) with a TGA 2950 thermobalance from TA Instruments operated in the high-resolution dynamic mode with an instrumen-tal resolution of five and 5 °C/min as the upper limit for the heating rate. IR spectra were recorded with a Perkin–Elmer instrument by the attenuated total reflectance (ATR) technique. UV/Vis spectra were recorded by the integration-sphere method. Zero-field-cooling (ZFC) and field-cooling (FC) magnetic curves were recorded in the 2–300 K temperature range with an MPMS magnetometer from Quantum Design. FC curves were recorded under an applied field of 50 Oe. Deconvolutions of sets of single peaks for the ν(OH) spec-tral region of the IR spectra and for the optical transitions present in the UV/Vis/NIR spectra were performed with the Fityk software.[27]

H_2 excess adsorption isotherms up to 4000 Torr (ca. 5 bar) were recorded with an ASAP 2050 analyzer (from Micromeritics). Sample tubes of known weight were loaded with the sample (60–70 mg) and sealed with Tran Seal. Before the H_2 adsorption, the samples were degassed (activated) in the ASAP analyzer at a heating rate of 1 °C/min in the temperature regime selected for the TG curves. In all cases, the degassing temperature was maintained until the out-gas rate was stabilized below 10^{-6} Torr. The degassed sample and sample tube were weighed and then transferred back to the analy-zer with the Tran Seal to prevent exposure to air. After volume-free measurement with helium, the sample was heated under vacuum for ca. 30 min at the activation temperature and then degassed for ca. 12 h. Details of the degassing process and the adsorption data processing are available in the Supporting Information. The H_2 ad-sorption measurements were performed at 75 K with a bath of liquid N_2. The relatively low temperature of liquid N_2 (75 K) corre-sponds to a local atmospheric pressure of 586 Torr.

The crystal structures of the six solids were refined from their pow-der XRD patterns recorded at room temperature with Cu-$K_{\alpha1}$ radia-tion in the Bragg–Brentano geometry with a Bruker D8 diffractome-ter. The reported structure for the series $Zn_3A_2[M(CN)_6]_2 \cdot xH_2O$ was used as the structural model to be refined.[7d,7e] Peak profiles were calculated within ten times the full width at half-maximum (FWHM). The background was modeled by a third-order polynomial equa-tion. The interatomic C–N and M–C distances were constrained to values within the limit considered in previous structural studies of analogous solids.[7d] Further details of the crystal structure investi-gations may be obtained from the Fachinformationszentrum Karls-ruhe, 76344 Eggenstein-Leopoldshafen, Germany (fax: +49-7247-808-666; e-mail: crysdata@fiz-karlsruhe.de), on quoting the file numbers CSD-431448 {for $Co_3(H_3O)_2[Ru(CN)_6]_2 \cdot 7.9H_2O$}, -431447 {for $Co_3(H_3O)_2[Ru(CN)_6]_2 \cdot 5.8H_2O$}, -431446 {for $Co_3(H_3O)_2[Os(CN)_6]_2 \cdot 8.4H_2O$}, -431445 {for $(H_3O)_2[Os(CN)_6]_2 \cdot 6.8H_2O$}, -431450 {for $Zn_3(H_3O)_2[Ru(CN)_6]_2 \cdot 5.2H_2O$}, and -431449 {for $Zn_3(H_3O)_2[Os(CN)_6]_2 \cdot 6.9H_2O$}.

Computational Details: The bulk of the $T_3(H_3O)_2[M(CN)_6]_2 \cdot uH_2O$ compounds were simulated with the primitive unit cell. Each com-putational cell was formed of two formula units and six cavities. Four of the pores were filled randomly with hydronium counter-cations, and the remaining cavities were filled with one water mol-ecule each to keep the model as simple and symmetric as possible. The lattice parameters, cell volume, and internal coordinates were allowed to relax fully during the geometry optimizations.

All calculations were performed within the spin-polarized density functional theory (DFT) framework as implemented in the Vienna Ab-initio Simulation Package (VASP).[28] The Kohn–Sham valence states were expanded in a plane-wave basis set with a cutoff fixed at 520 eV for the kinetic energy. The electron-exchange correlation was denoted by the generalized gradient approximation (GGA) in

the form of the Perdew–Burke–Ernzerhof functional revised for sol-ids (PBEsol).[29] The projector-augmented wave (PAW) method was used to describe the core orbitals and their interactions with the valence electrons.[30] The frozen core consisted of orbitals up to and including the 1s for the period-two elements, 3p for the period-four elements, 4s for Ru, and 4f for Os. The partial occupancies for all calculations were determined by the tetrahedron method with Blöchl corrections.[31] The DFT+U[32] approach by Dudarev et al.[33] was included to improve the description of the localized and strongly correlated d(Co) electrons. The effective Hubbard parame-ter (U_{eff}) value of 6.0 eV for the Co atom was determined by fitting the calculated band gap to the experimental one. We performed a set of DFT+U calculations in which U_{eff} was changed in steps of 0.5 eV from 0 to 6.5 eV, and the geometries were allowed to relax fully. As the calculations underestimated the experimental band gaps for the Zn-based compounds by 0.15–0.46 eV, we postulated a correction for the Co-based materials. We scaled down the band gap for $Co_3(H_3O)_2[Ru(CN)_6]_2$ according to Equation (2).

$$E_g^{cor}(Co_3(H_3O)_2[Ru(CN)_6]_2) = \frac{E_g^{cal}(Zn_3(H_3O)_2[Ru(CN)_6]_2) \cdot E_g^{exp}(Co_3(H_3O)_2[Ru(CN)_6]_2)}{E_g^{exp}(Zn_3(H_3O)_2[Ru(CN)_6]_2)}$$

(2)

Here, all of the compounds are in the S phase, and the cor, cal, and exp superscripts represent the corrected, calculated, and experi-mental band-gap energies, respectively.

All calculations included long-range dispersion corrections through the method of Grimme (D3) with a Becke–Jonson damping,[34] which is required for the accurate simulation of the interactions of adsorbates with extended surfaces[35] or internal cavities.[36] A Γ-centered Monkhorst–Pack grid of 3 × 3 × 3 k-points was used to sample the Brillouin zone integrations.[37] The conjugate-gradient minimization technique was used for geometry optimizations. The systems were considered converged when the Hellmann–Feynman forces on each ion fell below 0.1 eV/Å. The energy threshold defin-ing the self-consistency of the electron density was set at 10^{-5} eV. A larger cutoff for the kinetic energy of the plane waves, denser k-point meshes, and a lower self-consistent energy threshold were tested to ensure that the energies were converged within 1 meV per atom.

We tested different orientations for the magnetic spin moments of the transition-metal atoms to identify the ground state. Several combinations of low- and high-spin states equivalent to different initial magnetic moments were also carefully checked. The mag-netic moments were allowed to relax during each of the simula-tions. Atomic charges (and spin moments) were derived through Bader analysis[38] to quantify the charge transfer between the cyanometallate pores and the water molecules.

Supporting Information (see footnote on the first page of this article): Spectroscopic, magnetic, and structural information; refined atomic positions; occupation and isotropic thermal factors; calcu-lated interatomic distances and bond angles.

[1] a) K. W. Chapman, P. D. Southon, C. L. Weeks, C. J. Kepert, *Chem. Commun.* **2005**, 3322–3324; b) S. S. Kaye, J. R. Long, *J. Am. Chem. Soc.* **2005**, *127*, 6506–6507; c) K. W. Chapman, P. J. Chupas, E. R. Maxey, J. W. Richard-son, *Chem. Commun.* **2006**, 4013–4015; d) L. Reguera, J. Balmaseda, L. F. del Castillo, E. Reguera, *J. Phys. Chem. C* **2008**, *112*, 5589–5597; e) L. Reguera, J. Balmaseda, C. P. Krap, M. Avila, E. Reguera, *J. Phys. Chem. C* **2008**, *112*, 17443–17449; f) L. Reguera, C. P. Krap, J. Balmaseda, E. Re-guera, *J. Phys. Chem. C* **2008**, *112*, 15893–15899.

[2] a) M. Verdaguer, A. Bleuzen, V. Marvaud, J. Vaissermann, M. Seuleiman, C. Desplanches, A. Scuiller, C. Train, R. Garde, G. Gelly, C. Lomenech, I. Rosenman, P. Veillet, C. Cartier, F. Villain, *Coord. Chem. Rev.* **1999**, *190–192*, 1023–1047; b) R. Martínez-García, L. Reguera, M. Knobel, E. Reguera, *J. Phys. Condens. Matter* **2007**, *19*, 056202; c) C. Avendano, M. G. Hilfiger, A. Prosvirin, C. Sanders, D. Stepien, K. R. Dunbar, *J. Am. Chem. Soc.* **2010**, *132*, 13123–13125; d) M. Presle, I. Maurin, F. Maroun, R. Cortés, L. Lu, R. Sayed Hassan, E. Larquet, J.-M. Guigner, E. Riviére, J. P. Wright, J.-P. Boilot, T. Gacoin, *J. Phys. Chem. C* **2014**, *118*, 13186–13195; e) O. N. Risset, P. A. Quintero, T. V. Brinzari, M. J. Andrus, M. W. Lufaso, M. W. Meisel, D. R. Talham, *J. Am. Chem. Soc.* **2014**, *136*, 15660–15669.

[3] a) J. Balmaseda, E. Reguera, J. Rodríguez-Hernández, L. Reguera, M. Autie, *Microporous Mesoporous Mater.* **2006**, *96*, 222–236; b) S. S. Kaye, J. R. Long, *Catal. Today* **2007**, *120*, 311–316; c) J. Roque, E. Reguera, J. Balma-seda, J. Rodríguez-Hernández, L. Reguera, L. F. del Castillo, *Microporous Mesoporous Mater.* **2007**, *103*, 57–71; d) B. Zamora, J. Roque, J. Balma-seda, E. Reguera, *Z. Anorg. Allg. Chem.* **2010**, *636*, 2574–2578.

[4] a) S. Ohkoshi, K. Nakagawa, K. Tomono, K. Imoto, Y. Tsunobuchi, H. Tok-oro, *J. Am. Chem. Soc.* **2010**, *132*, 6620–6621; b) E. Perez-Cappe, M. Agui-lar-Frutis, N. Chavez, J. Ribalta, E. Reguera, *Microporous Mesoporous Ma-ter.* **2012**, *163*, 326–333; c) L. Shen, Z. Wang, L. Chen, *Chem. Eur. J.* **2014**, *20*, 12559–12562; d) Y. Yue, A. J. Binder, B. Guo, Z. Zhang, Z.-A. Qiao, C. Tian, S. Dai, *Angew. Chem. Int. Ed.* **2014**, *53*, 3134–3137; *Angew. Chem.* **2014**, *126*, 3198; e) J. Song, L. Wang, Y. Lu, J. Liu, B. Guo, P. Xiao, J.-J. Lee, X.-Q. Yang, G. Henkelman, J. B. Goodenough, *J. Am. Chem. Soc.* **2015**, *137*, 2658–2664.

[5] a) M. Avila, L. Reguera, J. Rodríguez-Hernández, J. Balmaseda, E. Reguera, *J. Solid State Chem.* **2008**, *181*, 2899–2907; b) J. Jiménez-Gallegos, J. Rod-ríguez-Hernández, H. Yee-Madeira, E. Reguera, *J. Phys. Chem. C* **2010**, *114*, 5043–5048.

[6] R. Martinez-Garcia, M. Knobel, E. Reguera, *J. Phys. Condens. Matter* **2006**, *18*, 11243.

[7] a) P. Gravereau, E. Garnier, A. Hardy, *Acta Crystallogr., Sect. B* **1979**, *35*, 2843–2848; b) E. Garnier, P. Gravereau, A. Hardy, *Acta Crystallogr., Sect. B* **1982**, *38*, 1401–1405; c) P. Gravereau, E. Garnier, *Rev. Chim. Miner.* **1983**, *20*, 68–77; d) J. Rodríguez-Hernández, E. Reguera, E. Lima, J. Balmaseda, R. Martínez-García, H. Yee-Madeira, *J. Phys. Chem. Solids* **2007**, *68*, 1630–1642; e) M. Avila, L. Reguera, C. Vargas, E. Reguera, *J. Phys. Chem. Solids* **2009**, *70*, 477–482.

[8] C. Rodríguez, E. Reguera, M. Ávila, *J. Phys. Chem. C* **2010**, *114*, 9322–9327.

[9] S. M. Holmes, G. S. Girolami, *J. Am. Chem. Soc.* **1999**, *121*, 5593–5594.

[10] J. Rodríguez-Carvajal, *Full Prof 2005 Program*, Institute Louis Brillouin, Saclay, **2005**.

[11] F. J. Torres, J. G. Vitillo, B. Civalleri, G. Ricchiardi, A. Zecchina, *J. Phys. Chem. C* **2007**, *111*, 2505–2513.

[12] G. Yang, Y. Wang, D. Zhou, X. Liu, X. Han, X. Bao, *J. Mol. Catal. A* **2005**, *237*, 36–44.

[13] R. L. Frost, R.-A. Wills, J. T. Kloprogge, W. N. Martens, *J. Therm. Anal. Calorim.* **2006**, *83*, 213–218.

[14] J. M. Headrick, E. G. Diken, R. S. Walters, N. I. Hammer, R. A. Christie, J. Cui, E. M. Myshakin, M. A. Duncan, M. A. Johnson, K. D. Jordan, *Science* **2005**, *308*, 1765–1769.

[15] E. Reguera, J. Fernández-Bertrán, J. Duque, *Polyhedron* **1994**, *13*, 479–484.

[16] A. B. P. Lever, *Inorganic Electronic Spectroscopy*, 2nd ed., Elsevier, New York, **1984**.

[17] J. M. Zadrozny, J. Telser, J. R. Long, *Polyhedron* **2013**, *64*, 209–217.

[18] J. C. Wojdel, S. T. Bromley, *J. Phys. Chem. B* **2006**, *110*, 24294–24298.

[19] a) J. Tauc, R. Grigorovici, A. Vancu, *Phys. Status Solidi A* **1966**, *15*, 627–637; b) J. Tauc, F. Abeles, *Optical Properties of Solids*, vol. 372, North-Holland, Amsterdam, **1972**.

[20] P. Kubelka, F. Munk, *Z. Tech. Phys.* **1931**, *12*.

[21] O. Kahn, *Molecular Magnetism*, VCH, New York, **1993**.

[22] H. Sakiyama, *J. Chem. Software* **2001**, *7*, 171–177.

[23] D. Santos-Carballal, A. Roldan, R. Grau-Crespo, N. H. de Leeuw, *Phys. Rev. B* **2015**, *91*, 195106.

[24] a) G. J. Kubas, *Chem. Rev.* **2007**, *107*, 4152–4205; b) T. K. A. Hoang, L. Morris, J. Sun, M. L. Trudeau, D. M. Antonelli, *J. Mater. Chem. A* **2013**, *1*, 1947–1951.

[25] E. Reguera, *Int. J. Hydrogen Energy* **2009**, *34*, 9163–9167.

[26] G. Brauer (Ed.), *Handbook of Preparative Inorganic Chemistry*, vol. 2, 2nd ed., Academic Press, New York, **1965**.

[27] M. Wojdyr, http://www.unipress.waw.pl/fityk (accessed on May 12, **2009**].

[28] a) G. Kresse, J. Hafner, *Phys. Rev. B* **1993**, *47*, 558–561; b) G. Kresse, J. Hafner, *Phys. Rev. B* **1994**, *49*, 14251–14269; c) G. Kresse, J. Furthmüller, *Phys. Rev. B* **1996**, *54*, 11169–11186.

[29] J. P. Perdew, A. Ruzsinszky, G. I. Csonka, O. A. Vydrov, G. E. Scuseria, L. A. Constantin, X. Zhou, K. Burke, *Phys. Rev. Lett.* **2008**, *100*, 136406.

[30] a) P. E. Blöchl, *Phys. Rev. B* **1994**, *50*, 17953–17979; b) G. Kresse, D. Jou-bert, *Phys. Rev. B* **1999**, *59*, 1758–1775.

[31] P. E. Blöchl, O. Jepsen, O. K. Andersen, *Phys. Rev. B* **1994**, *49*, 16223–16233.

[32] V. I. Anisimov, M. A. Korotin, J. Zaanen, O. K. Andersen, *Phys. Rev. Lett.* **1992**, *68*, 345–348.

[33] S. L. Dudarev, G. A. Botton, S. Y. Savrasov, C. J. Humphreys, A. P. Sutton, *Phys. Rev. B* **1998**, *57*, 1505–1509.

[34] a) S. Grimme, J. Antony, S. Ehrlich, H. Krieg, *J. Chem. Phys.* **2010**, *132*, 154104; b) S. Grimme, S. Ehrlich, L. Goerigk, *J. Comput. Chem.* **2011**, *32*, 1456–1465.

[35] a) D. Santos-Carballal, A. Roldan, R. Grau-Crespo, N. H. d. Leeuw, *Phys. Chem. Chem. Phys.* **2014**, *16*, 21082–21097; b) D. Santos-Carballal, A. Roldan, N. H. d. Leeuw, *J. Phys. Chem. C* **2016**, *120*, 8616–8629.

[36] C. E. Hernandez-Tamargo, A. Roldan, N. H. d. Leeuw, *J. Phys. Chem. C* **2016**, *120*, 19097–19106.

[37] H. J. Monkhorst, J. D. Pack, *Phys. Rev. B* **1976**, *13*, 5188–5192.

[38] a) R. F. W. Bader, *Atoms in Molecules: A Quantum Theory*, Oxford University Press, Oxford, **1990**; b) G. Henkelman, A. Arnaldsson, H. Jónsson, *Comput. Mater. Sci.* **2006**, *36*, 354–360; c) E. Sanville, S. D. Kenny, R. Smith, G. Henkelman, *J. Comput. Chem.* **2007**, *28*, 899–908; d) W. Tang, E. Sanville, G. Henkelman, *J. Phys. Condens. Matter* **2009**, *21*, 84204.